# 8 Three–dimensional lithography of Photonic Crystals

*Alvaro Blanco, Kurt Busch, Markus Deubel, Christian Enkrich, Georg von Freymann, Martin Hermatschweiler, Wolf–Peter Koch, Stefan Linden, Daniel C. Meisel, and Martin Wegener*[1]

## 8.1 Introduction

The publications of Yablonovitch [1] and John [2] in 1987 on the optical properties of three–dimensional (3D) periodic structures have triggered an enormous interest in the scientific community. They predicted that the electromagnetic modes in Photonic Crystals (PhCs) are strongly influenced by the periodic variation of the dielectric constant. For certain symmetries and material compositions, Bragg scattering leads to the formation of a complete photonic band gap (PBG). This is a frequency range in which the propagation of electromagnetic waves in the 3D PhC is forbidden for any wave vector and polarization. Accordingly, Bragg scattering opens a PBG in the direction or plane of periodicity for appropriate one–dimensional (1D) or two–dimensional (2D) structures.

The excitement about PhCs is based partially on the prospect of "molding the flow of light" by intentionally introducing defects in the crystal structure [3]. These defects give rise to localized photonic states inside the PBG and can be used as functional elements for photonic devices. For example, a microcavity can be implemented by a point defect and a line defect constitutes a waveguide. Compared to their conventional counterparts, these elements can be realized on a much smaller scale based on PhCs. Ultimately, the goal is to make use of the interplay between PBGs and defect modes to create integrated photonic circuits.

So far, this field of research is mainly driven by progress in the theoretical description of light in PhCs and by the development of more efficient numerical methods. On the experimental side, insufficient quality of the PhCs is still a mayor issue. The problems of sample fabrication are associated with the fact that the lattice constant of a PhC has to be on the order of half the wavelength of light in the material. While this does not represent a big challenge in the microwave regime — in this case, one can literally drill holes in a slab of material [4] — things are much harder in the telecommunications window and the visible spectral region.

Electron beam lithography and selective etching processes have been used for the fabrication of 2D PhCs. The most common designs consist of periodically structured slab waveguides [5]. Another successful approach is to fabricate 2D PhCs with a large aspect ratio based on macroporous silicon [6]. On account of their exceptional quality, 2D PhCs have been used for many experiments in the near–infrared. Nevertheless, there is a principal drawback. 2D PhCs do not possess a complete PBG and therefore are only suited for a limited set of applications. For example, it is not possible to suppress the spontaneous emission in all directions

[1]Corresponding author, e-mail: martin.wegener@physik.uni-karlsruhe.de

*Photonic Crystals.* Edited by K. Busch, S. Lölkes, R. B. Wehrspohn and H. Föll
Copyright © 2004 Wiley-VCH Verlag GmbH & Co. KGaA
ISBN: 3-527-40432-5

within a 2D PhC. For the same reason, these structures are also prone to scattering losses in the third dimension which ultimately restricts their performance.

Since electron beam lithography is a planar technique, it is not straightforward to transfer this method to the fabrication of 3D PhCs. A possible way to overcome this problem is to fabricate samples based on a layer–by–layer design [7,8]. In a first step, the surface of a wafer is processed with the above mentioned techniques. The next layer is then added either by deposition and subsequent patterning of a dielectric film or by bonding two pieces of the wafer followed by removal of one of the substrates. This procedure is repeated several times until the desired number of layers is reached. In practice, PhCs made by the layer–by–layer method are limited by the complexity of the fabrication process to only a few periods. Additionally, a high degree of mechanical precision is required to avoid offsets between the different layers.

So far, the most common method to produce 3D PhCs is based on self–assembly of sub–micrometer spheres. Here one takes advantage of the natural tendency of monodisperse spheres to form a face–centered cubic (fcc) lattice during segregation [9]. In nature, this process leads to the formation of opals. This gemstone is also the eponym for artificial crystals assembled by self–organization. Unfortunately, a fcc lattice of dielectric spheres does not have a complete PBG. The inverted structure, a fcc lattice of air spheres in a dielectric medium, on the other hand has a complete PBG, provided the refractive index of the medium is larger than 2.8 [10]. This inversion process can be accomplished, for example, by chemical vapour deposition (CVD) and subsequent selective etching of the opal template. Silicon inverted opals with a complete PBG centered at $1.46\ \mu\mathrm{m}$ have been demonstrated [11]. However, inverted opals are extremely sensitive to disorder. It has been predicted [12], that deviations in sphere size as small as $2\%$ will result in a destruction of the complete PBG. The fragility of the PBG can be attributed to the fact that the PBG is rather small and is located between the eighth and ninth band in the high–frequency range of the band structure. This poses severe demands on the synthesis of the colloidal spheres and on the uniformity of the inversion process.

Our approach to 3D PhC fabrication comprises two different lithographic methods: Holographic lithography and direct laser writing. These optical methods, which are highly qualified for the production of top–quality polymeric 3D PhCs, are described in detail in Section 8.2 and 8.3. Scanning electron microscope (SEM) micrographs and optical spectra of samples made by our group are presented in either case. Since the refractive index of the used polymer is only 1.6, a supplementary inversion process of the polymeric PhCs with a high refractive index material is necessary to open up a complete PBG. Our roadmap to accomplish this task is outlined in Section 8.4.

## 8.2 Holographic lithography

Light fields resulting from multiple beam interference have been studied in detail for the purpose of trapping and cooling of atoms [13]. Such fields are also of great interest for the fabrication of PhCs since the light distribution can be spatially periodic or quasi–periodic with a period on the order of half the wavelength. The interference pattern can be recorded as a volume hologram and converted into a correspondingly structured matter distribution. The resulting material, in principle, can serve as a PhC because its refractive index varies accordingly [14–17].

Photoresists are used as recording medium. In the following, we describe how to fabricate materials periodically structured in 3D on a wavelength scale by holographic lithography. These structures can also serve as templates for PhCs.

### 8.2.1 The photoresist

Essentially two kinds of photoresists are in use with cationic or radical polymerization. In radical-curing systems, absorption of light generates free radicals that initiate polymerization processes. Radical systems are sensitive to oxygen which must be excluded, otherwise the polymerization can be affected severely. Therefore the material must be processed in an inert atmosphere or protected by some other means. For a detailed comparison with cationic systems cf. [18].

This problem is absent in cationic systems. An often used representative of this group is the commercially available thick film photoresist SU-8 (sold by MicroChem Corporation). It consists of an octafunctional epoxy resin (EPON® SU–8), a photoinitiator (mixed Triarylsulfonium/Hexafluoroantimonate salt in propylene carbonate solvent), both dissolved in gamma–butyrolactone (GBL) [19, 20]. The photoinitiator generates an acid upon irradiation by near UV light ($350 - 400$ nm). The spatial acid concentration is an image of the irradiation dose. In a post–exposure bake, the latent picture is converted into a cross–linking density by a chain reaction during thermal treatment at $65°$ to $93°$ C for several minutes.

The cross–linking degree determines the solubility in the "developing" solvent. GBL or another appropriate solvent are used in this step. Thus, sufficiently illuminated resin remains ("negative" photoresist) whereas underexposed resin is washed away. The remaining material therefore has a shape that follows the surface for the threshold irradiation, which is the boundary between over– and under–exposed regions. Effectively, the interference pattern is stored in a digitized form: It is a porous air–polymer–structure showing the isodose surface for the threshold dose value.

A "positive" photoresist requires a resin that upon irradiation undergoes chemical changes that make it soluble [19]. When a positive photoresist is illuminated with the same interference pattern the inverted structure is obtained as compared to a negative photoresist.

### 8.2.2 The crystallography of multiple-beam interference patterns

It is of importance to predict the structure that is obtained for a given beam configuration. The respective calculations allow one to systematically study the influence of the experimental parameters like beam directions, intensities and polarizations on the resulting structure. Because of the threshold dose feature of the photoresist process, the quantities of interest are the isodose surfaces. The mathematics for the intensities suggests to make use of the laws developed for crystallographic purposes.

The interfering light beams are treated as plane waves with the electric field vector as the real part of a complex quantity:

$$\vec{E}_n(\vec{r},t) = \mathrm{Re}\{\vec{E}_n^0 e^{i(\vec{k}_n\cdot\vec{r}-\omega t)}\} \qquad \text{with integer } n = 1,\ldots,N \tag{8.1}$$

In what follows it is assumed that the $N$ beams are obtained by splitting one beam, i. e. all $|\vec{k}_n|$ are the same. The exposure dose $\mathcal{D}(\vec{r})$ is proportional to the light intensity (meant as

time–averaged Poynting vector) of the superposition of the $N$ waves. It can be expressed as a Fourier sum [14, 15, 21] according to

$$\mathcal{D}(\vec{r}) \propto \left| \sum_{n=1}^{N} \vec{E}_n^0 \, \mathrm{e}^{\mathrm{i}(\vec{k}_n \cdot \vec{r} - \omega t)} \right|^2 = \sum_{n,m=1}^{N} a_{nm} \, \mathrm{e}^{\mathrm{i}\vec{G}_{nm} \cdot \vec{r}} \tag{8.2}$$

The (generally complex) "form factors" $a_{nm} := \vec{E}_n^0 \cdot \vec{E}_m^{0^*}$ result from the relative amplitudes, polarizations and phases of the light beams. It has to be noted that the Fourier sum results in a real quantity. The differences $\vec{G}_{nm} := \vec{k}_n - \vec{k}_m$ of the wave vectors in essence result from the relative directions of the beams.

**Translational symmetry**

The representation of $\mathcal{D}(\vec{r})$ as a Fourier sum (8.2) is the same as that one describing the periodicity of a crystal [22]; it relates the spatial behavior of $\mathcal{D}(\vec{r})$ in real space $\vec{r}$ to vectors $\vec{G}_{nm}$ in reciprocal space. As usual in crystallography, the existence of a set of primitive basis vectors $\{\vec{b}_i\}$ for the set $\{\vec{G}_{nm}\}$ allows one to conclude that the interference pattern has lattice properties.

The number of basis elements $\{\vec{b}_i\}$ gives the dimensionality $d$ of the reciprocal lattice. For $d = 2$, the five 2D Bravais lattices are at choice. If $d$ turns out to be 3, one of the 14 3D Bravais lattices applies. All 14 Bravais lattices can be generated by four noncoplanar beams [23]. Four beams constitute the minimal set allowing for the fabrication of 3D periodic structures. Adding further beams in general destroys the lattice property unless they fit to the lattice already present [13].

The corresponding real space lattice with basis $\{\vec{a}_i\}$ follows from the condition:

$$\vec{b}_i \cdot \vec{a}_j = 2\pi\delta_{ij} \tag{8.3}$$

with $\delta_{ij}$ as the Kronecker delta. In 3D periodic systems the solution is:

$$\vec{a}_1 = 2\pi \frac{\vec{b}_2 \times \vec{b}_3}{\vec{b}_1 \cdot (\vec{b}_2 \times \vec{b}_3)} \qquad \text{and cyclic permutations of the indices.} \tag{8.4}$$

Under special circumstances the lattice can degenerate to lower dimensionality through the form factors. Pathological cases have to be considered separately.

A phase shift of one beam with respect to the others, in general, leads to another pattern. Under special conditions the topology of the interference pattern is phase independent and the interference pattern is shifted in space only [13].

At present, the favorite lattice type for a full PBG is a fcc lattice [1, 10]. The respective reciprocal lattice is body–centered cubic (bcc). For this reason all $\vec{G}_{mn}$ occurring in sum (8.2) have to lie on a bcc lattice. One choice for a realization is the so–called "umbrella–like" beam configuration with 4 beams as described below (Section 8.2.3).

**The basis element of the structure**

Given a lattice, the structure repeated at every lattice point in real space is called "basis element"; it is the structure inside a Wigner–Seitz cell (WSC). In solid state crystallography, this

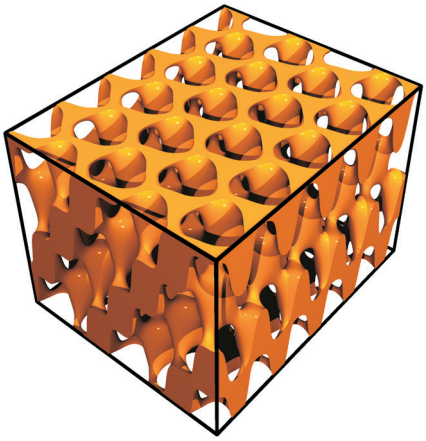

**Figure 8.1:** Simulation of a fcc structure with a filling factor $f = 0.29$ [21]. Four beams are arranged in a so–called "umbrella–like" configuration. A detailed description with parameter values is given in Section 8.2.3.

corresponds to the electron density at a lattice point. For a given lattice type (i. e. for fixed directions of the $\vec{k}_n$) the shape and volume of the basis element is determined by the form factors $a_{nm}$ and thus by both, the intensities and the polarizations of the beams. The filling factor $f$ is the volume of the basis element divided by the volume of the WSC.

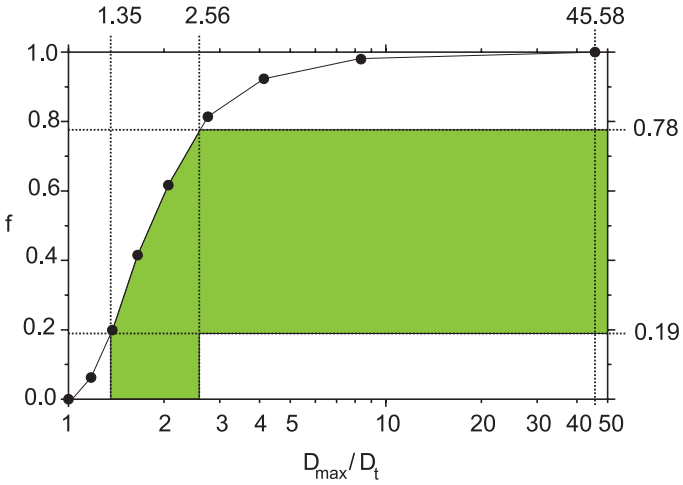


**Figure 8.2:** Computed filling factor $f$ of our fcc structures (see Fig. 8.1) as a function of the exposure dose $\mathcal{D}_{\max}/\mathcal{D}_{\mathrm{t}}$. $\mathcal{D}_{\max}$ is the maximum dose occurring in the interference pattern and $\mathcal{D}_{\mathrm{t}}$ is the threshold dose of the photoresist [21]. Useful material requires $\mathcal{D}_{\max}/\mathcal{D}_{\mathrm{t}}$ to be between 1.35 and 2.56 or $f$ between 0.19 and 0.78 (shaded green). More details are given in the text.

All features of the resulting structure can be calculated using (8.2) to find the isosurface for a certain threshold dose value (see Fig. 8.1). As an example, a question of practical importance is studied numerically: To obtain a structure that is of practical use, it must be mechanically stable, i. e., the basis elements have to be interconnected, otherwise the structure falls apart. On the other hand, the underexposed regions have to be interconnected, too. This is required to make sure that the pores are washed out by the developer. For this purpose the structure was calculated for different exposure doses, i. e. for different filling factors. Figure 8.2 shows the result of this calculation for the fcc structures described in Section 8.2.3. It gives the filling factor $f$ as a function of the peak dose $\mathcal{D}_{\max}$ occurring in the interference pattern. $\mathcal{D}_{\max}$ in turn is given in units of the threshold dose $\mathcal{D}_{\mathrm{t}}$. Below $\mathcal{D}_{\max}/\mathcal{D}_{\mathrm{t}} = 1$ no regions

are sufficiently illuminated, resulting in $f = 0$. If the minimum dose $\mathcal{D}_{\min}$ reaches $\mathcal{D}_{\rm t}$ all material is fully exposed, i. e. $f = 1$. This is the case for $\mathcal{D}_{\max}/\mathcal{D}_{\rm t} \geq 45.58$. Only in the range $\mathcal{D}_{\max}/\mathcal{D}_{\rm t} = 1.35 \ldots 2.56$ are both interconnectivity conditions simultaneously fulfilled. From $\mathcal{D}_{\max}/\mathcal{D}_{\rm t} = 1.35$ on, the basis elements are interconnected and above $\mathcal{D}_{\max}/\mathcal{D}_{\rm t} = 2.56$ the pores are closed. The corresponding filling factors are 0.19 and 0.78. It is to be noted that in the useful range ($\mathcal{D}_{\max}/\mathcal{D}_{\rm t} = 1.35 \ldots 2.56$) the dose varies by less than a factor of two [21].

### 8.2.3 Experimental realization

The SU-8 photoresist solution is spun on a glass substrate and heated to $95^\circ$ C for several minutes for drying ("soft bake"). A hard photoresist layer of about $10\ \mu$m thickness is obtained.

A frequency-tripled Nd:YAG laser at $355$ nm wavelength is used as light source (model GCR 170–10 by Spectra-Physics). This Q-switched laser emits pulses of $6$ ns duration so that any problems due to mechanical vibrations during exposure are avoided. In order to make the laser oscillant on a single longitudinal mode only it is seeded. The beam diameter is about $8$ mm.

The output of the laser is split into four beams, the polarization and intensities of which can be adjusted independently. A 3D periodic interference pattern is produced by the so–called "umbrella–like" configuration [24]: One beam (central beam $\#1$) is made perpendicular to the photoresist layer. The three other beams are equally distributed on a cone with beam $\#1$ on the cone axis (cf. Fig. 8.3a). The apex angle $\gamma$ of the cone determines the lattice type which in general is trigonal.

The central beam is circularly polarized while the others are linearly p–polarized. The energy ratios of beam $\#1 : \#2 : \#3 : \#4$ are $1.5 : 1 : 1 : 1$. After a single laser shot exposure the sample is heated ("post–exposure bake") to fully cure the overexposed regions.

Thereafter the underexposed regions are dissolved in the developer liquid. Figure 8.3 shows a SEM image of a sample with an internal angle $\gamma_{\rm tri} = 22.82^\circ$ which results in a trigonal structure.

A fcc lattice requires an internal apex angle of $\gamma_{\rm fcc} = \arccos(7/9) = 38.94^\circ$ [24]. This angle is not directly accessible since the refraction of the beams at the air photoresist interface has to be taken into account. The index of refraction limits the angles $\gamma$ inside the photoresist layer to values below the critical angle of total internal reflection which is $36.78^\circ$ for SU–8.

In order to solve this problem, the light is coupled through a fused silica prism into the photoresist layer. We use a corner cube prism with a chopped–off tip for this purpose. The coupling from the prism into the photoresist is through a water immersion film. To get $\gamma_{\rm fcc} = 38.94^\circ$ inside the photoresist layer, $\gamma_{\rm air}$ in air has to be $40.36^\circ$ taking into account the corner cube geometry [21].

Figure 8.4 shows a SEM picture of a true fcc sample [17]. Due to the shrinkage of the structure during polymerization by about $7.5\,\%$ [25] the lattice constant $a_{\rm fcc}$ (length of the cubic cell) of the fcc structure including the shrinkage is calculated to be $509$ nm.

Due to shrinkage the samples tend to crack and to peel off the substrate. Both effects can be reduced considerably by surrounding the porous samples with narrow frames of fully polymerized bulk material. The frames are prepared by illuminating the SU–8 film with a UV lamp while the area inside the frames is protected by an appropriately patterned mask [21]. Thereafter the film is exposed to the interfering laser beams. After heat treatment and

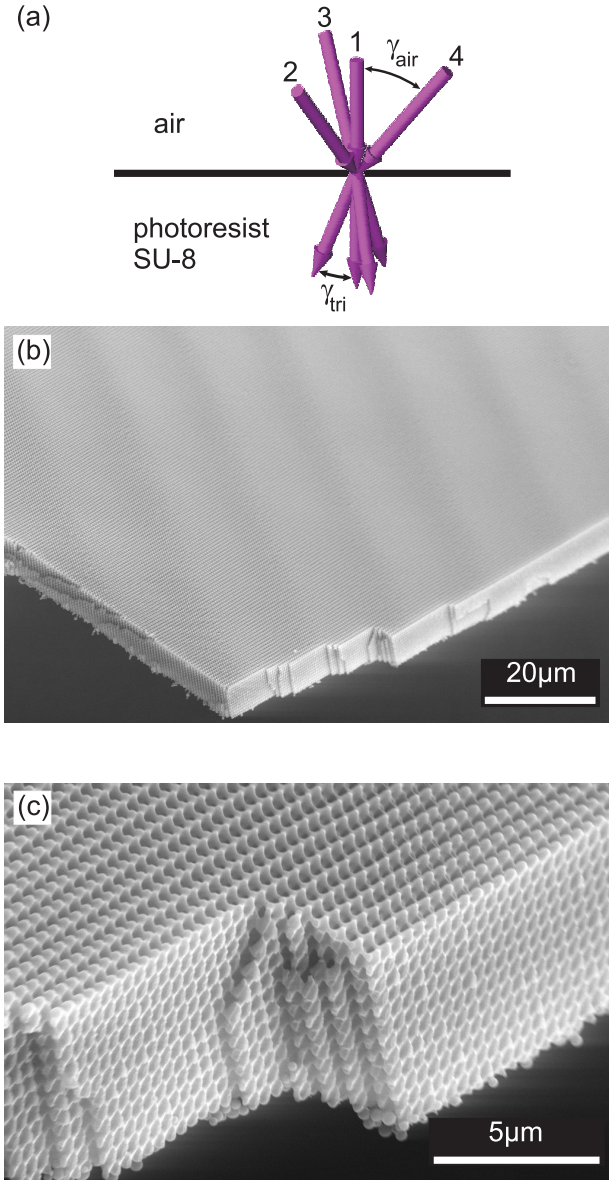


**Figure 8.3:** (a) The "umbrella–like" configuration with beam #1 perpendicular to the photoresist surface and the remaining beams equally distributed on the surface of a cone with an apex angle $\gamma_{\rm air} = 40.36^\circ$ in air. Due to refraction at the air–photoresist interface, the angle inside the photoresist layer is smaller ($\gamma_{\rm tri} = 22.83^\circ$) resulting in a trigonal structure. (b) and (c) are SEM images of an edge of the trigonal structure obtained for the values as of (a) for two magnifications.

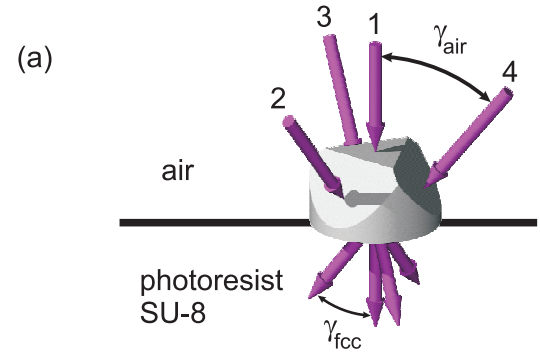


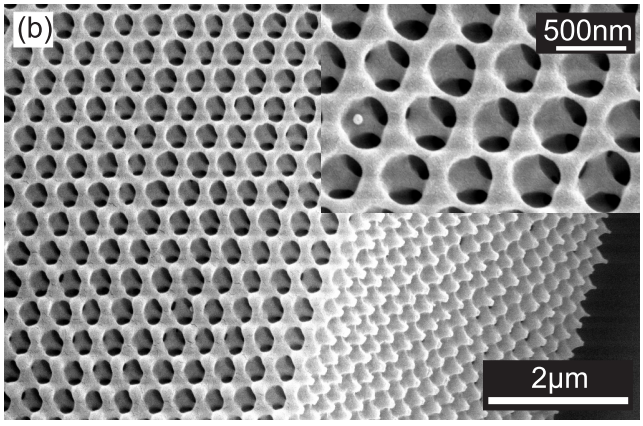


**Figure 8.4:** (a) The "umbrella–like" configuration including the coupling prism. An angle $\gamma_{\rm air} = 40.36^\circ$ in air leads to the necessary angle of $\gamma_{\rm fcc} = 38.94^\circ$ inside the photoresist required for a fcc structure. The beams are coupled through a water film into the photoresist. (b) SEM images of the fcc structure. The inset is a closeup showing the hexagonal pattern of a (111) net plane of the fcc structure. The filling factor is estimated to be 0.29 (cf. Fig. 8.1).

development, the porous regions are held by the surrounding frames which adhere well to the substrate. Mesh widths of $50\ \mu$m to $500\ \mu$m have been used successfully so far.

### 8.2.4 Optical properties of the photoresist structures

In order to enable band structure calculations and to interpret measured data, the index of refraction for polymerized bulk SU–8 for 633 nm is determined by measuring Brewster's angle. The index is found to be $n = 1.61$. By comparing the SEM images visually with computer simulations (see Fig. 8.1) the filling factor is estimated to be 0.29 [21].

The optical properties of fcc structures fabricated by holography were studied by means of both transmission and reflection experiments. The experimental setup allows focusing of the incident beam in a region smaller than $100\ \mu$m (typically $50\ \mu$m). This is very important due to the actual geometry of the samples and also to check their homogeneity in short range.

Figure 8.5 is a combination of measured transmission data along the (111) direction with a corresponding band structure calculation. It shows a reasonable agreement between the measured transmission dip and the calculated stop band position and width in $\Gamma$-L direction [17].

In the reflection experiments, white light is sent onto the sample at normal incidence with respect to the (111) face and the specular reflectance is collected, using a beam splitter, in the detector. The transmission experiment allows us as well to explore the dependence of

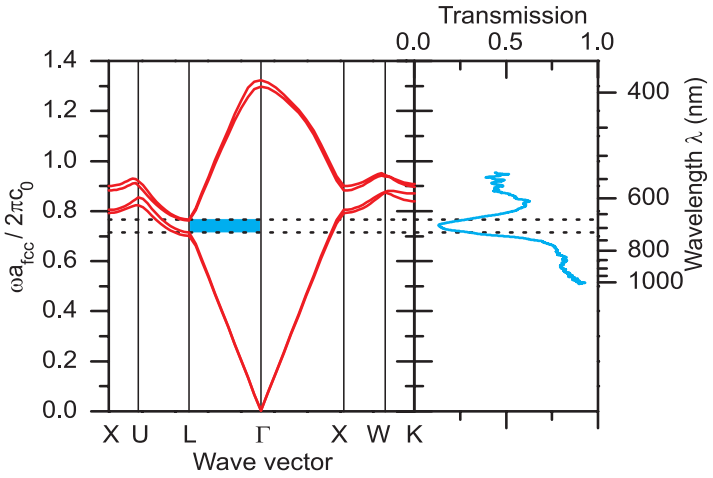


**Figure 8.5:** Calculated band structure (left) and transmission spectrum in the (111) direction (Γ-L) (right) for the structure shown in Fig. 8.4. The measured position and width of the dip is in fair agreement with the calculations. At 680 nm the transmission drops to 15 %.

the optical properties with respect to the incidence angle $\theta$, which is a must to fully characterize any PhC structure. In Fig. 8.6a the transmission for different angles of incidence ($\theta = 0° \ldots \theta = 55°$) is shown. At normal incidence, the wave vector is parallel to the Γ–L direction. As $\theta$ increases we move away from Γ–L to other crystal directions following either L–U, L–W or L–K. The spectral evolution of the Bragg peak, here a dip, can easily be followed as $\theta$ increases (see 8.6a and b).

The value of transmission measurements is that every single photon missing is taken into account as a dip in the transmitted intensity. Reflection measurements, on the other hand, are only sensitive for specularly reflected light while photons scattered in other directions are not recorded. This allows the observation of higher energy features which can be related with other crystal directions [26] or higher photonic bands.

## 8.3 Direct laser writing

Holographic lithography of PhC structures can easily produce samples with defect–free areas of several square millimeters and offers a high flexibility in tailoring the unit cell. Due to the fabrication principle, these structures are strictly periodic, i.e., defect structures cannot be included in a controlled fashion. However, the controlled fabrication of defect structures, such as microcavities or waveguides, in otherwise defect–free PhCs is essential for many technological applications. Therefore, an additional method to introduce defect structures into the holographic PhC templates has to be applied.

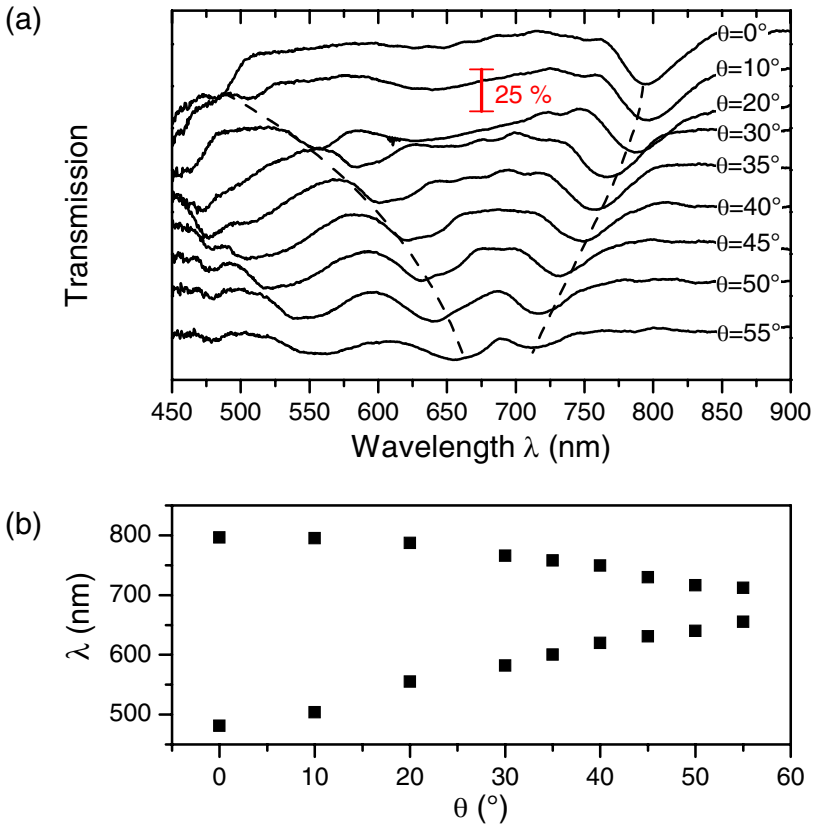


**Figure 8.6:** (a) Transmission spectra of a fcc structure fabricated by holographic lithography for different angles of incidence $\theta$. At normal incidence, the wave vector is parallel to the Γ-L direction. The individual curves are vertically displaced for clarity. The dashed lines are guides to the eye in order to follow the spectral evolution of the transmission minima. (b) Spectral position of the transmission minima for different angles of incidence $\theta$.

### 8.3.1 Multi–photon polymerization

Conventional photolithographical microstructuring of photosensitive materials is a well established technique to convert patterns of light into physical structures. However, structures fabricated by this method are mostly 2D as the absorption of light in the photosensitive media proceeds from the illuminated surface to the substrate. 3D arrangements may be formed by layer–by–layer techniques, where after exposure and structuring of one layer, this layer is lowered in a bath of liquid photoresist, and a second layer is exposed on top of the first. By sequentially repeating this process, 3D multilayer structures can be fabricated. Besides the limitations of structure size, this concept is not applicable to the problem considered here,

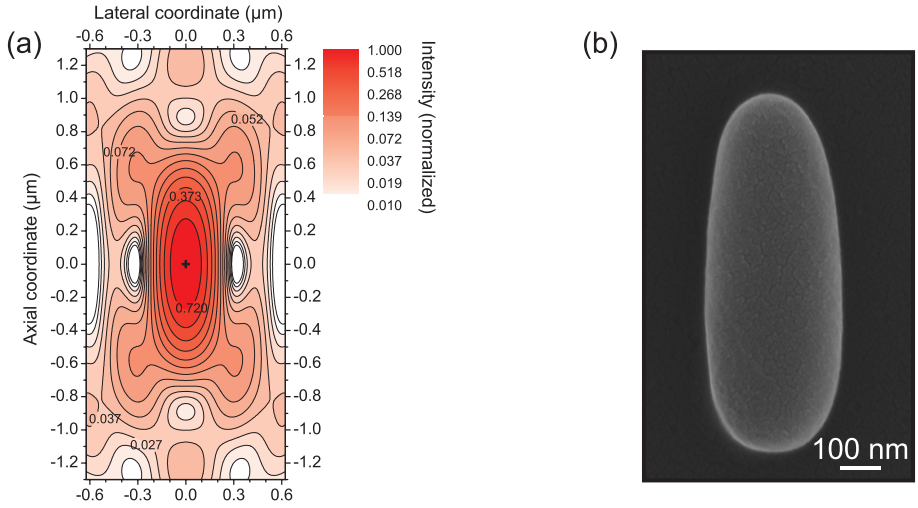


**Figure 8.7:** (a) Calculated isophotes of the microscope objective used in our experiments (for calculational model see [39]; $NA = 1.4$, $\lambda = 800$ nm, polarization perpendicular to lateral coordinate). The intensity is normalized to the value in the origin (geometrical focus). (b) Voxel exposed by a single laser pulse.

where defect structures need to be fabricated *inside* PhC templates: A writing method is required which itself provides 3D resolution.

A technique that is able to accomplish this task and which is especially suitable for polymeric PhCs is 3D direct laser writing (DLW) by multi–photon polymerization [27–29].

For colloidal PhCs, where the integration of defect structures is a similar problem, two–photon absorption DLW has already been demonstrated successfully for the writing of waveguide structures inside self–assembled opal templates [30].

Multi–photon absorption (MPA) DLW may also be used for the fabrication of complete 3D PhC lattices. Several groups have reported the fabrication of such structures in photoresists [28, 31–35] and silica glass [36], [37].

In MPA DLW, photosensitive threshold systems, mostly photoresists exhibiting an intensity threshold for exposure, are illuminated by laser light that has insufficient photon energy to expose the photosensitive medium by a one–photon absorption process. When the laser light is sharply focused into the medium, however, the light intensity near the focus may become sufficiently high to exceed the exposure threshold by multi–photon processes. As the probability of these processes scales with $I^n$ where $I$ is the light intensity and $n$ the number of photons involved in the absorption process, the exposed region is confined to a small volume element ("voxel") inclosing the focus, whereas the rest of the medium remains unexposed. By scanning the focus relative to the medium, in principle, any 3D structure may be written directly into the photosensitive medium.

The size and shape of the exposed voxels depend on the isodose surfaces, the isophotes, of the microscope objective and the multi–photon exposure threshold of the photosensitive medium. The calculated isophotes of the microscope objective that is used in our experiments

are shown in Fig. 8.7a. The isophotes in the vicinity of the geometrical focus exhibit a typical near–elliptical shape. The aspect ratio, i.e. the ratio between the axial and the lateral diameter of a voxel, strongly depends on the numerical aperture $NA$ of the microscope objective. Since the ellipticity decreases for larger $NA$, mostly oil–immersion objectives with the highest numerical apertures currently available are used for DLW.

Figure 8.7a seems to suggest that the size of a voxel may be chosen arbitrarily small: Given a particular exposure threshold by the photosensitive medium, the whole volume inside the corresponding isophote will be exposed upon illumination. If one simply reduces the light intensity, this value will move to isophotes closer and closer to the geometrical focus, resulting in smaller and smaller voxels. Ultimately, the smallest feature size would be limited by the physical and chemical resolution of the photosensitive medium. In practice, it is the stability of the laser light intensity that determines the smallest reproduceably writable structures, as the susceptibility to fluctuations of the isophote–distribution increases strong, close to the geometrical focus.

Nevertheless, MPA DLW offers the possibility of sub–diffraction limited resolution for the 3D structuring of photosensitive media. A spatial resolution of $120\ \mathrm{nm}$ at a fabrication wavelength of $780\ \mathrm{nm}$ has been reported (lateral structure size), which corresponds to $\lambda/6.5$ [29].

## 8.3.2 Experimental realization

### Photoresist

We use SU–8 negative photoresist in the DLW fabrication process (see Section 8.2.1), as the compatibility of the photoresist systems for holography and DLW is crucial. When utilizing the same resist, DLW may simply be added as a second exposure step to the holographic fabrication process prior to development of the PhC. Additionally, the cationic polymerization mechanism of SU–8 is of great advantage, since the monomers do not polymerize directly after exposure. Therefore, the difference in the refractive indices of exposed and unexposed photoresist is negligible and structures that have already been exposed will not affect further exposure steps. Another advantage is that SU–8 is solid during the writing process. This does not only make the sample handling much more comfortable, but also offers a higher degree of freedom in the scanning pattern, since successively written structures do not have to be interconnected immediately.

Like many other commercially available photoresists, SU–8 has a rather low sensitivity for multi–photon absorption (MPA). Therefore, sharp focusing of laser light alone is insufficient to surpass the MPA threshold. To supply sufficiently high intensities, pulsed laser sources are necessary. For femtosecond (fs) laser pulses, it has been reported that even single shot exposure of SU–8 is possible [38]. This can be a great advantage in terms of writing time, as the polymerization in most resist systems currently in use for DLW relies on multishot exposure of single voxels.

### Experimental setup

Prior to exposure, a $20\ \mu\mathrm{m}$ thick SU–8 photoresist film is spin coated on a coverslide and solidified by a soft–bake process. The laser, a regeneratively amplified Ti:sapphire laser system

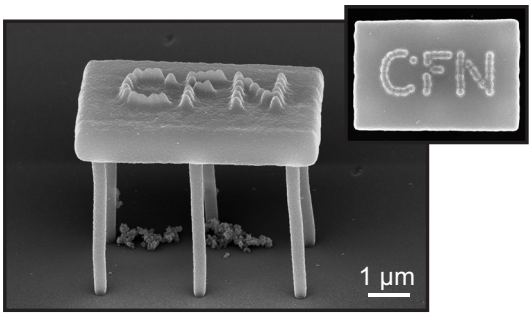


**Figure 8.8:** 3D structure fabricated by DLW: Logo of the DFG–Center for Functional Nanostructures.

(Spectra Physics Hurricane, pulse duration 120 fs, repetition rate adjustable from single shot mode to 1 kHz) is tuned to a central wavelength of 800 nm, where the one–photon absorption of SU–8 is negligible [38]. The beam is attenuated by a halfwave–plate/polarizer combination and after beam expansion coupled into a custom designed inverted microscope (Leica). The beam is then focused into the photoresist by a $100\times$ oil–immersion microscope objective ($NA = 1.4$). The inverted microscope allows a prepositioning of the substrate relative to the spatially fixed focal spot of the laser beam. This substrate is held in a three–axis piezoelectric scanning stage (Physik Instrumente) that is operated in closed loop and reaches a resolution of 5 nm at a full scanning range of 200 $\mu$m $\times$ 200 $\mu$m $\times$ 20 $\mu$m. A personal computer controls the scanning operation of the piezo stage and synchronizes its movement with the pulsing of the laser system via a laser controlling interface. After DLW of a preprogrammed pattern, the exposed sample is postbaked and developed as described in Section 8.2.3 for the holographic PhC templates.

Figure 8.7b shows a single voxel that has been polymerized by a single laser pulse. Its near-elliptical shape corresponds quite nicely to the calculated intensity distribution for our optical system and shows the typical aspect ratio of about 2.7 for the microscope objective employed here. This shape now forms the basic building block for all fabricated structures shown in this article. The diameter of the single voxels can be adjusted by changing the laser pulse energy from about 2 $\mu$m (higher pulse energies lead to evaporation of the unpolymerized SU–8) to less than 200 nm. In structures consisting of connected voxels, the single voxel distance can be used as an additional degree of freedom to adjust the structural details. In Fig. 8.8, the logo of the DFG–Center for Functional Nanostructures written on a table of only 6 $\mu$m side length, shows the high flexibility and accuracy of our 3D writing.

### 8.3.3 Direct laser writing of three–dimensional photonic crystals

Because of their simple geometrical structure, the so–called layer–by–layer [40] or woodpile [41] PhCs are ideal structures for DLW.

Figure 8.9 shows a schematical drawing of the design of this group of PhCs: Layers consisting of straight parallel rods with a center–to–center distance $a$ are stacked to a 3D lattice. Adjacent layers have the orientation of the rods rotated by $90^\circ$ and second nearest neighbouring layers are shifted by a distance of $a/2$ perpendicular to the rod axes. This stacking sequence repeats itself after every four layers with a lattice constant $c$. For $c/a = \sqrt{2}$, this 3D lattice has a fcc primitive unit cell with a basis of two rods, and face centered tetragonal

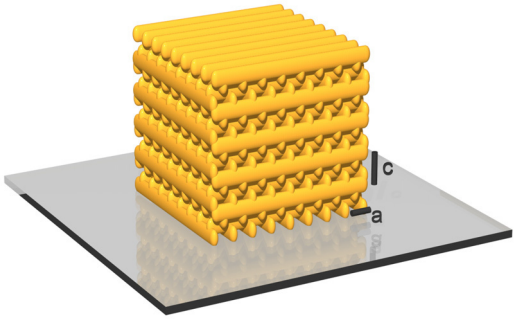


**Figure 8.9:** The layer–by–layer or woodpile structure: Straight parallel rods with an axis–distance $a$ form layers that are stapled into a 3D lattice. The stacking sequence repeats itself after every four layers.

(fct) symmetry otherwise. Its structure can be derived from the diamond lattice by replacing the (110)–chains by the straight rods [40]. Theoretical calculations by Ho et al. [40] have shown, that such PhCs can have a complete PBG for an index contrast as small as $1.9$. It is located between the second and third band, and has a gap/midgap ratio of up to $28\ \%$ for air rods in silicon. In addition to that, various rod cross sections, filling fractions and overlapping of adjacent layers show sizeable PBGs. Further calculations by Chutinan et al. [42] predict that these structures are also relatively insensitive to structural imperfections.

Layer–by–layer structures have already been fabricated by DLW in photosensitive polymers that exhibit PBGs at mid– and near–infrared wavelengths [28, 31–35]. As the refractive index of the employed polymers is approximately $1.5$, these structures have no complete PBG.

Figure 8.10 shows two 20–layer structures that have been fabricated with our setup. The cross–section of the individual rods is elliptical which is a direct consequence of the single voxel shape. For means of stability, adjacent layers need to overlap to a certain extent. The single voxel distance here was chosen, still large enough, to keep the single voxels distinguishable. In the inset, the nanometer–scale roughness on the surface of the single voxels shows the physical resolution of the resist itself.

In order to do optical experiments on such samples, the area of the structures needs to be increased. Figure 8.11a shows a sample consisting of 32 layers with an area of $70\ \mu\mathrm{m} \times 70\ \mu\mathrm{m}$. The in–plane rod distance $a$ is $0.8\ \mu\mathrm{m}$ and $c/a$ is adjusted to $\sqrt{2}$ for fcc symmetry. To reduce lattice distortions and sample bending due to polymer shrinkage, a massive wall has been polymerized around the PhC structure by the same technique. Although this is quite a large structure for DLW with that resolution, the writing time of the PhC lattice is just $25$ minutes with a scanning algorithm optimized for the layer–by–layer structures.

To check that the sample quality is not just restricted to the surface, and to make sure that the development process also leads to a porous structure inside the PhC, a sample with 12 layers was broken through the middle of the structure. Fig. 8.11 (b) shows SEM images of the top and an edge view of the sample that indicate that also the interior of the layer–by–layer PhC matches the designed structure.

With the highly flexible DLW technique, it is now possible to write a wide variety of lattice constants and filling fractions by changing the scanning pattern and the laser pulse energy

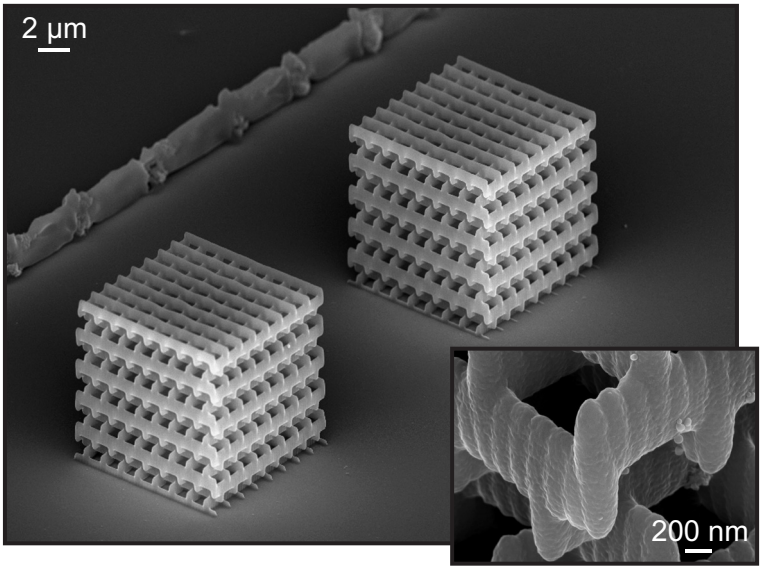


**Figure 8.10:** SEM image of two layer–by–layer structures with $a = 1.5\ \mu\mathrm{m}$; total size is $12\ \mu\mathrm{m} \times 12\ \mu\mathrm{m} \times 11\ \mu\mathrm{m}$. In the inset, the single voxels that build the rods can be distinguished. The surface roughness of the voxels is determined by the resolution of the resist itself.

respectively. Figure 8.12 shows an overview over several structures that we have fabricated. All lattices were designed with $c/a = \sqrt{2}$ for fcc symmetry. The in–plane rod distance $a$ here ranges from a rather large $1.5\ \mu\mathrm{m}$ down to $650\ \mathrm{nm}$. The images reveal the precise large–scale periodicity as well as the high fabrication accuracy even for small lattice constants.

### 8.3.4 Optical characterization

We have performed optical transmission and reflection measurements on layer–by–layer samples consisting of six lattice constants and an effective area of $100\ \mu\mathrm{m} \times 100\ \mu\mathrm{m}$. The transmission and reflection spectra are measured in a Fourier Transform Infrared Spectrometer (Hartmann–Braun Bomen) combined with an infrared microscope (SpectraTech, $15\times$ Cassegrain objectives, $NA = 0.56$, aperture size $50\ \mu\mathrm{m} \times 50\ \mu\mathrm{m}$). The samples are aligned with their surfaces perpendicular to the optical axis, which corresponds to $\Gamma$-X direction for fcc symmetry. The spectra are normalized to the glass substrate in the case of transmission and to a gold mirror in the case of reflection. Figure 8.13 shows the dataset of a sample with an in–plane rod distance of $a = 1.0\ \mu\mathrm{m}$. The fundamental stop band at about $1.9\ \mu\mathrm{m}$ is clearly visible, both in reflection and transmission, as well as a higher order stop band at $1.1\ \mu\mathrm{m}$. The presence of this higher order stop band displays the high optical quality of the sample.

Figure 8.14 compares the reflection spectra of three other samples with different in–plane rod distances. As expected, a pronounced shift of the stop band towards higher energies with decreasing rod distance can be observed. The maximum of the reflection shifts from $1.9\ \mu\mathrm{m}$

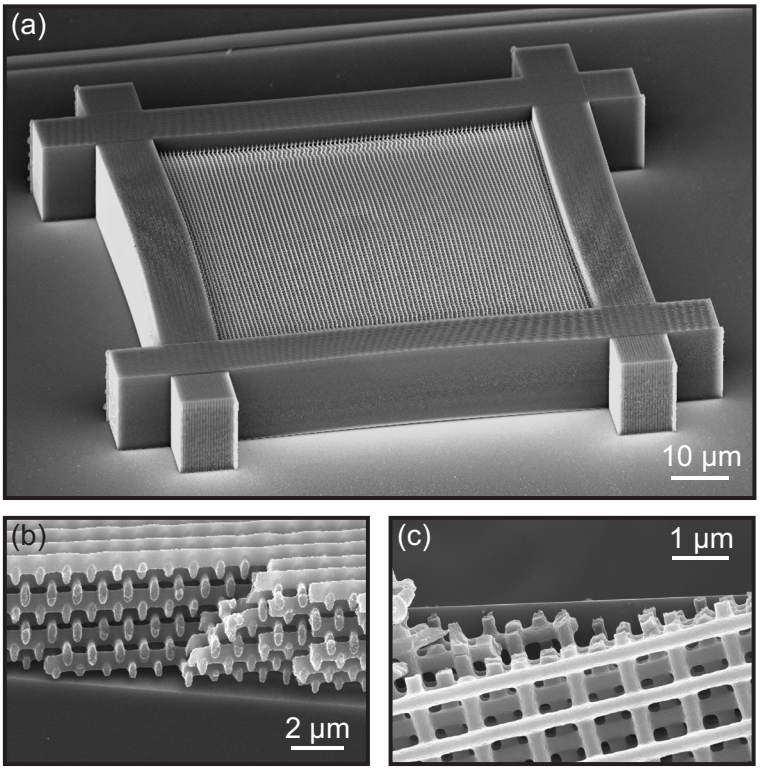


**Figure 8.11:** (a) Larger layer–by–layer structure with a massive wall that prevents bending and reduces lattice distortions due to polymer shrinkage during polymerization. (b) Side and (c) top view of a broken sample with 12 layers that exhibit the sample quality inside the structures.

for the $a = 1.0\ \mu$m–sample to $1.4\ \mu$m for $a = 0.8\ \mu$m. For the sample with $a = 1.0\ \mu$m, again the reflection peak of the higher–order stop band is visible and even more pronounced than the respective one of the fundamental stop band. For the $a = 0.9\ \mu$m–sample, a rise in the reflection also hints at the existence of a higher–order stop band, but due to the spectral shift, it does not fall into the measured spectral window.

## 8.4 Templates infiltration

SU–8 fcc periodic structures do not possess a full PBG. However, a number of very interesting applications are just related to their photonic properties and not to the full gap itself: anomalous propagation is caused by the unique features coming from the shape of the photonic bands (equienergy surfaces) and leads to interesting phenomena such as superprism effects [43], or negative refraction [44]; in nonlinear optics, a full PBG is not required to efficiently produce second harmonic generation [45]. Nevertheless, the "Holy Grail", the so–called complete PBG is a must to mold the flow of light. Waveguides, microcavities, engineered defects,

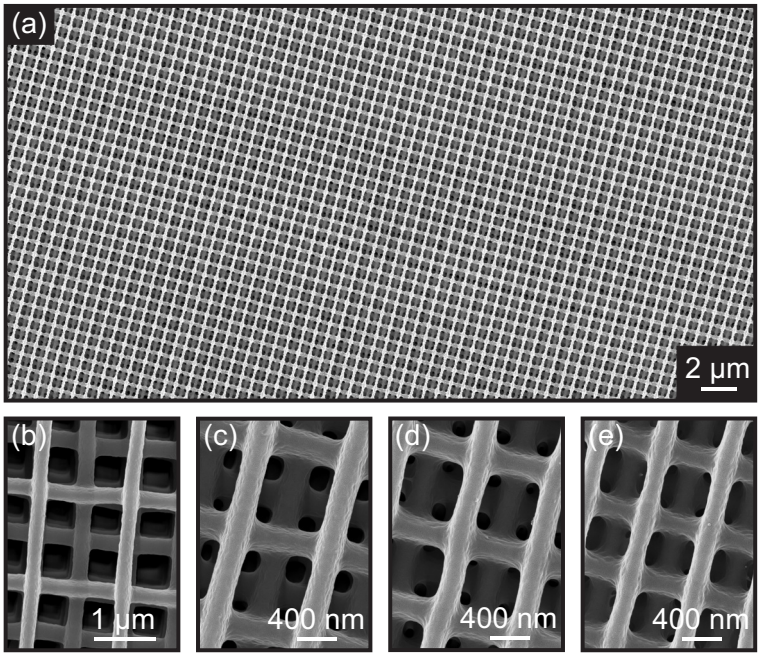


**Figure 8.12:** (a) The overview of a sample with $a = 0.65\ \mu\mathrm{m}$ reveals the large scale periodicity of our samples, whereas closeups for samples with different $a$ exhibit the small scale fabrication accuracy: (b) $a = 1.5\ \mu\mathrm{m}$, (c) $a = 1.0\ \mu\mathrm{m}$, (d) $a = 0.8\ \mu\mathrm{m}$, (e) $a = 0.65\ \mu\mathrm{m}$.

spontaneous emission inhibition and other fundamental quantum optical effects are related, or linked to the existence of a full PBG.

In this way, the SU–8 fcc structures can be seen as templates where other compounds with higher dielectric constant can be grown into, in order to achieve the dielectric contrast that is theoretically predicted. In the holographic structures, materials such as silicon, germanium, III–V semiconductors, etc., with refractive indices higher than 2.8 are good candidates to overcome this problem. In the layer-by-layer structures, this threshold is lower due to their diamond symmetry. Therefore, the list of appropriate materials is larger. The different techniques that can be used depend on the material to grow: chemical vapor deposition (CVD) for silicon [11] and germanium [46], electrodeposition, which has been used for II–VI [47] and III–V [48] semiconductors, chemical bath deposition [49], etc.

### 8.4.1 Silicon CVD

Infiltration by silicon CVD is a standard technique, which is commonly used for the fabrication of inverted opals. In contrast to the artificial opal templates that consist of silica spheres and can be inverted with silicon directly, the temperature stability of SU–8 raises a major problem: Experiments on our structures have shown that for temperatures above $250^\circ$ C, the SU–8 structures lose their mechanical integrity. As the silicon CVD works at temperatures above

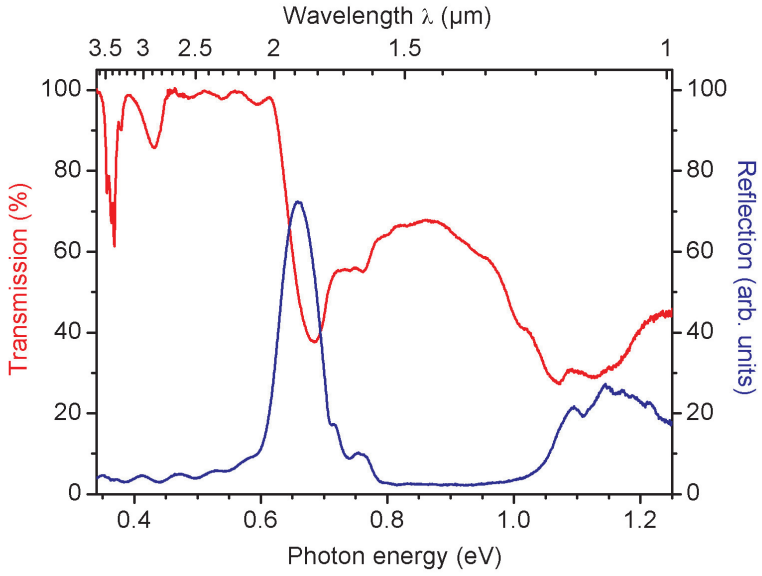


**Figure 8.13:** Transmission and reflection spectra of our $a = 1.0\ \mu\mathrm{m}$ layer–by–layer structures. The transmission dips around $3\ \mu\mathrm{m}$ and $3.5\ \mu\mathrm{m}$ stem from polymer absorption bands.

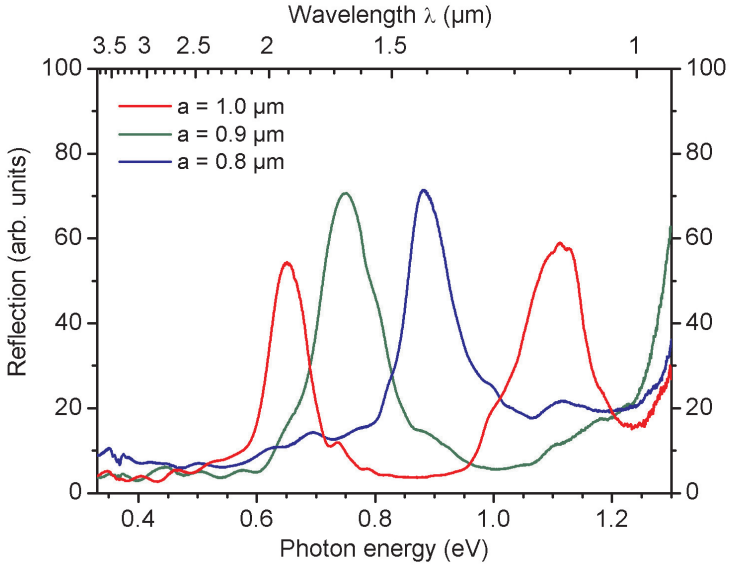


**Figure 8.14:** Reflection spectra of samples with different in–plane rod distance $a$.

$350^\circ$ C, the method has to be adapted for our templates. This procedure will be sketched for the case of the layer–by–layer templates next.

In an initial step, the layer–by–layer templates and their substrate are covered with a thin polymer layer. The structural changes caused by this layer are negligible since the deposited layer is less than $5$ nm thick. Next, the templates are completely inverted with silica ($SiO_2$) in a process which can be accomplished at room temperature and thus leaves the structure unaffected [50]. For this purpose, the templates are first dried in a stream of nitrogen gas and followed by the addition of a defined amount of water which is physiosorbated. The water reacts in the next step with $SiCl_4$ and forms a $30 - 40$ nm thick layer of $SiO_2$. By repeating these steps several times, the templates are completely infiltrated with $SiO_2$.

After the infiltration, the template as well as the substrate are completely covered with $SiO_2$. In order to remove the SU–8 a new substrate is placed on top of the layer–by–layer structure. Since the old substrate was covered with a polymer film before the $SiO_2$ CVD, it can be removed easily. A direct burn–up of the SU–8 could destroy the moulded $SiO_2$ structure if the flue gases are not dissipated fast enough. Therefore, drains in the residual polymer film and in the SU–8 are opened beforehand by exposing the sample to an oxygen–plasma. After that, the sample is heated up to $500^\circ$ C for 4 hours which removes the remaining resist.

The resulting $SiO_2$-inverted template is compatible with the silicon CVD process. Here, the sample is heated up to $375^\circ$ C at an ambient pressure of $10^{-6}$ mbar. Disilane ($Si_2H_6$) gas is added to the reaction chamber which decomposes on the surface of the inverted template due to the high temperature. This leads to the formation of a silicon layer whose thickness is monitored by a sensing crystal. After the silicon CVD process, the $SiO_2$ is removed with an aqueous solution of hydrofluoric acid.

### 8.4.2 Electrochemical deposition

So far, transparent materials with low intrinsic losses in the spectral region of interest are prefered for the fabrication of PhCs. However, compound structures of dielectric materials and metals have been proposed [51] as an interesting alternative to all-dielectric PhCs for some applications. These systems can be useful to study the interaction between light and surface plasmons in nanostructured metals, a topic which has gained much attention in the last few years [52]. Even all-metallic photonic structures with very interesting properties in the infrared region [53] have been demonstrated.

Electrodeposition is a versatile technique suitable for the infiltration of our SU–8 PhC templates with metals or other materials. For this purpose, we are currently developing a computer controlled electrodeposition setup which comprises a standard three–electrode configuration. By exchanging the counter electrode and the electrolyte, different materials can be utilized. The applied potential can either be held constant or can be varied with time in a controlled manner. In order to check the deposition conditions, a voltammogram can be measured before the real electrochemical deposition process.

Clearly, a conductive substrate is required for the electrodeposition process. Unfortunately, coating the substrate with a thin metal film is not compatible with the holographic fabrication process of the SU–8 templates since the metal coating gives rise to unwanted reflections. A good alternative is the use of indium–tin–oxide (ITO). We have deposited ITO

layers which are at the same time almost transparent and exhibit a sufficient conductance for the electrodeposition process.

The deposition of silver in the voids of the SU–8 templates is currently under way. The first results are very promissing.

## 8.5 Conclusions

We have shown that the combination of two complementary and compatible techniques, namely holographic lithography and Laser Direct Writing, allows the rapid, flexible and cheap fabrication of 3D PhC templates as well as the controlled incorporation of defects and waveguides. The optical transmission and reflection spectra of these structures in the visible and near–infrared respectively agree well with theory, which is evidence of the high quality of the fabricated structures. The next logical step and challenge is the infiltration of these structures with dielectrics with large refractive indices and/or with metals. Our corresponding first results along the lines of electrochemistry and, alternatively, CVD are very encouraging. It should be noted that the combination of such 3D nanolithography with e.g. CVD, is compatible with possible future mass production of 3D PhCs.

## References

[1] E. Yablonovitch, Phys. Rev. Lett. **1987**, 58, 2059.
[2] S. John, Phys. Rev. Lett. **1987**, 58, 2486.
[3] J.D. Joannopoulos, R.D. Meade, and J.N. Winn, Photonic Crystals − Molding the Flow of Light, Princeton University Press, USA, 1995.
[4] E. Yablonovith, T.J. Gmitter, and K.M. Leung, Phys. Rev. Lett. **1991**, 67, 2295.
[5] T.F. Krauss, R.M. De La Rue, and S. Brand, Nature **1996**, 383, 699.
[6] A. Birner, R.B. Wehrspohn, U.M. Gösele, and K. Busch, Adv. Mater. **2001**, 13, 377.
[7] S.Y. Lin, J.G. Fleming, D.L. Hetherington, B.K. Smith, R. Biswas, K.M. Ho, M.M. Sigalas, W. Zubrzycki, S.R. Kurtz, and J. Bur, Nature **1998**, 394, 251.
[8] S. Noda, K. Tomoda, N. Yamamoto, and A. Chutinan, Science **2000**, 289, 604.
[9] Y. Xia, B. Gates, and Z.H. Li, Adv. Mater. **2001**, 13, 409.
[10] K. Busch and S. John, Phys. Rev. E **1998**, 58, 3896-3908.
[11] A. Blanco, E. Chomski, S. Grabtchak, M. Ibisate, S. John, S.W. Leonard, C. Lopez, F. Meseguer, H. Miguez, J.P. Mondia, G.A. Ozin, O. Toader, and H.M. van Driel, Nature **2000**, 405, 437.
[12] Z.Y. Li and Z.Q. Zhang, Phys. Rev. B **2000**, 62, 1516.
[13] G. Grynberg and C. Robilliard, Phys. Rep. **2001**, 355, 335.
[14] V. Berger, O. Gauthier-Lafaye, and E. Costard, J. Appl. Phys. **1997**, 82, 60.
[15] M. Campbell, D.M. Sharp, M.T. Harrison, R.G. Denning, and A. J. Turberfield, Nature **2000**, 404, 53.
[16] S. Shoji and S. Kawata, Appl. Phys. Lett. **2000**, 76, 2668.
[17] Yu. V. Miklyaev, D.C. Meisel, A. Blanco, G. v. Freymann, K. Busch, W. Koch, C. Enkrich, M. Deubel, and M. Wegener, Appl. Phys. Lett. **2003**, 82, 1284.
[18] F. Sitek, M. Rembold, SME technical papers **1987**, FC870274.
[19] J.M. Shaw, J.D. Gelorme, N.C. LaBianca, W.E. Conley, and S. Holmes, IBM J. Res. Dev. **1997**, 41, 81.
[20] J.D. Gelorme, R.J. Cox, S.A.R. Gutierrez, U.S. Patent **1987**, No. 4, 882, 245.
[21] D.C. Meisel, Diploma Thesis, Universität Karlsruhe **2002**.

[22] C. Kittel, Introduction to solid state physics, John Wiley & Sons, 6th edition **1996**.
[23] L.Z. Cai, X.L. Yang, and Y.R. Wang, J. Opt. Soc. Am. A **2002**, 19, 2238.
[24] K.I. Petsas, A.B. Coates, and G. Grynberg, Phys. Rev. A **1994**, 50, 5173-5189.
[25] L.J. Guérin, M. Bossel, M. Demierre, S. Calmes, and P. Renaud, Proceedings of the International Solid State Sensors and Actuators Conference (Transducers '97) **1997**, 2, 1419.
[26] H. Miguez, C. Lopez, F. Meseguer, A. Blanco, L. Vazquez, R. Mayoral, M. Ocana, V. Fornes, and A. Mifsud, Appl. Phys. Lett. **1997**, 71, 1148.
[27] S. Maruo, O. Nakamura, and S. Kawata, Opt. Lett. **1997**, 22, 132.
[28] B.H. Cumpston, S.P. Ananthavel, S. Barlow, D.L. Dyer, J.E. Ehrlich, L.L. Erskine, A.A. Heikal, S.M. Kuebler, I.-Y.S. Lee, D. McCord-Maughon, J. Qin, H. Röckel, M. Rumi, X.-L. Wu, S.R. Marder, and J.W. Perry, Nature **1999**, 398, 51.
[29] S. Kawata, H.-B. Sun, T. Tanaka, and K. Takada, Nature **2001**, 412, 697.
[30] W. Lee, S.A. Pruzinsky, and P.V. Braun, Adv. Mater. **2002**, 14, 271.
[31] J. Serbin, A. Egbert, A. Ostendorf, B.N. Chichkov, R. Houbertz, G. Domann, J. Schulz, C. Cronauer, L. Fröhlich, and M. Popall, Opt. Lett. **2003**, 28, 301.
[32] M. Straub and M. Gu, Opt. Lett. **2003**, 27, 1824.
[33] H.-B. Sun, S. Matsuo, and H. Misawa, Appl. Phys. Lett. **1999**, 74, 786.
[34] H.-B. Sun, V. Mizeikis, Y. Xu, S. Juodkazis, J.-Y. Ye, S. Matsuo, and H. Misawa, Appl. Phys. Lett. **2001**, 79, 1.
[35] M.J. Ventura, M. Straub, and M. Gu, Appl. Phys. Lett. **2003**, 82, 1649-1651.
[36] H.-B. Sun, Y. Xu, S. Juodkazis, K. Sun, M. Watanabe, S. Matsuo, H. Misawa, and J. Nishii, Opt. Lett. **2001**, 26, 325.
[37] S. Juodkazis, S. Matsuo, H. Misawa, V. Mizeikis, A. Marcinkevicius, H.–B. Sun, Y. Tokuda, M. Takahashi, T. Yoko, and J. Nishii, Appl. Surf. Sci. **2002**, 197, 705.
[38] G. Witzgall, R. Vrijen, E. Yablonovitch, V. Doan, and B.J. Schwartz, Opt. Lett. **1998**, 23, 1745.
[39] A. Yoshida and T. Asakura, Optik **1974**, 41, 281-292.
[40] K.M. Ho, C.T. Chan, C.M. Soukoulis, R. Biswas, and M. Sigalas, Solid State Commun. **1994**, 89, 413.
[41] H.S. Sözüer and J.P. Dowling, J. Mod. Optic. **1994**, 41, 231.
[42] A. Chutinan and S. Noda, J. Opt. Soc. Am. B **1999**, 16, 240.
[43] H. Kosaka, T. Kawashima, A. Tomita, M. Notomi, T. Tamamura, T. Sato, and S. Kawakami, Phys. Rev. B **1998**, 58, R10096.
[44] C.Y. Luo, S.G. Johnson, J.D. Joannopoulos, and J.B. Pendry, Opt. Express **2003**, 11, 746.
[45] J. Martorell, R. Vilaseca, and R. Corbalan, Appl. Phys. Lett **1997**, 70, 702.
[46] H. Miguez, E. Chomski, F. Garcia-Santamaria, M. Ibisate, S. John, C. Lopez, F. Meseguer, J.P. Mondia, G.A. Ozin, O. Toader, and H.M. van Driel, Adv. Mater. **2001**, 13, 1634.
[47] P.V. Braun and P. Wiltzius, Nature **1999**, 402, 603.
[48] Y.C. Lee, T.J. Kuo, C.J. Hsu, Y.W. Su, and C.C Chen, Langmuir **2002**, 18, 9942.
[49] A. Blanco, C. Lopez, R. Mayoral, H. Miguez, F. Meseguer, A. Mifsud, and J. Herrero, Appl. Phys. Lett. **1998**, 73, 1781.
[50] H. Miguez, N. Tétreault, B. Hatton, S.M. Yang, D. Perovic, and G.A. Ozin, Chem. Commun. **2002**, 22, 2736.
[51] E.R. Brown and O.B. McMahon, Appl. Phys. Lett. **1995**, 67, 2138-2140.
[52] H.J. Lezec, A. Degiron, E. Devaux, R.A. Linke, L. Martin–Moreno, F.J. Garcia–Vidal, and T.W. Ebbesen, Science **2002**, 297, 820.
[53] J.G. Fleming, S.Y. Lin, I. El–Kady, R. Biswas, and K.M. Ho, Nature **2002**, 417, 52.